Electrochemical Proton Insertion Modulates the Hydrogen Evolution Reaction on Tungsten Oxides

Michael A. Spencer,[1] Jenelle Fortunato,[1] & Veronica Augustyn[1,*]

[1] Dept. of Materials Science and Engineering, North Carolina State University, Raleigh, NC USA 27695

*Corresponding author: Veronica Augustyn (vaugust@ncsu.edu)

ABSTRACT:

Development of new electrocatalysts for the hydrogen evolution reaction (HER) could reduce dependence on Pt and other rare metals and enable large-scale production of hydrogen with near-zero carbon emissions. Mechanistic insight into the electrocatalytic activity of a material helps to accelerate the development of new electrocatalysts. Alternative electrocatalyst materials such as transition metal oxides and sulfides can undergo insertion reactions that change their properties. Recent reports indicate that the presence of inserted ions can influence electrocatalytic activity. Here, we utilized a materials chemistry approach to understand the role of proton insertion on the HER activity of layered tungsten oxide hydrates ($WO_3 \cdot xH_2O$, x = 1, 2). We synthesized a series of tungsten oxide hydrates along with an octylamine-pillared tungsten oxide (OA-WO_3). We used cyclic voltammetry to study the electrochemical reactivity of each material and performed ex situ X-ray diffraction and Raman spectroscopy to understand bulk and surface structural changes during electrochemical cycling. We show an inverse relationship between the degree of proton insertion and HER overpotential in tungsten oxides: the lack of proton insertion leads to a high overpotential for the HER. We discuss three hypotheses for how proton insertion leads to HER activity in $WO_3 \cdot xH_2O$: 1) proton insertion changes the electronic band structure of $WO_3 \cdot xH_2O$, 2) the presence of bulk protons can influence $\Delta G_{H,ads}$ at the surface sites, and 3) inserted protons may participate in the HER mechanism on $WO_3 \cdot xH_2O$. Overall, this work shows the critical role of proton insertion in enabling high HER activity in tungsten oxides.

I. INTRODUCTION

Hydrogen is an important industrial element and energy-dense fuel used in the production of metals and chemicals as well as fuel cells.[1] Ten million metric tons, representing 14% of the global hydrogen, is produced in the US. The production of hydrogen with lower carbon emissions via electrolysis using electricity produced by nuclear or renewable energy could replace existing hydrogen production methods such as natural gas reforming. There are several technological hurdles to the wide-spread use of electrolysis for hydrogen production, including the need for low-cost, high activity, and durable electrocatalysts. The highest performing electrocatalysts for the hydrogen evolution reaction (HER) are platinum and the platinum group metals, but their material and processing costs hinder the widespread application in electrolyzers at a scale that would influence the hydrogen economy.[2,3] As a result, there are ongoing efforts to identify high performance, low-cost, and abundant electrocatalysts for the HER.[3] Transition metal oxides, sulfides, and phosphides are of interest as HER catalysts due to the tunability of their crystal structure, morphology, and electronic properties through doping or incorporation of defects.[4–6] Mechanistic understanding of the HER on such materials can inform material selection and accelerate development of high performance, economical electrocatalysts.[7] Moreover, mechanistic understanding of the HER on electrode surfaces helps in understanding more complex electrocatalytic reactions, such as those involving more than two electrons.

Given that many transition metal oxides and sulfides can undergo electrochemical proton and cation insertion, it is important to determine the role of this process on electrocatalysis. Electrochemical ion insertion can change the chemical, physical, and electronic structure of electrocatalysts and thus influence the electrochemical reaction mechanism. For example, Mefford et al. reported that the electrocatalytic activity of CoO_xH_y toward the oxygen evolution reaction (OER) was dependent on hydroxide ion (de)intercalation.[8] Hydroxide ion intercalation led to oxidation of Co and higher activity. Intercalated ions can also increase the electrocatalytic activity of layered transition metal sulfides toward the HER.[9–12] Gao et al. reported that titanates

intercalated with 3d transition metals exhibit lower overpotentials for catalyzing the HER.[12] Strong electronic interactions between the 3d transition metals and the [TiO_6] layers led to more favorable hydrogen adsorption free energies ($\Delta G_{H,ads}$) at surface oxygen sites. These reports show that the presence of ions in layered electrocatalysts can strongly influence the electrocatalytic reactivity.

Herein, we used a materials chemistry approach to understand the role of electrochemical proton insertion on the HER in a transition metal oxide by synthesizing a series of layered tungsten oxides, including a hybrid organic/inorganic material with no cation insertion ability, and characterizing their HER activity. We selected the tungsten oxide hydrate ($WO_3 \cdot xH_2O$; x = 1, 2) system for its ability to undergo fast and reversible proton insertion[13] and a semiconductor-to-metallic transition[14] during electrochemical cycling, making the electronic properties favorable for electrocatalysis. The interlayer water molecules in $WO_3 \cdot xH_2O$ can be replaced by organic pillars to modulate the capacity for proton and cation insertion. Our results show that a high overpotential is required to drive the HER when proton insertion is suppressed by the presence of organic pillars in tungsten oxide. Conversely, reversible proton insertion occurs in $H_xWO_3 \cdot xH_2O$, which is correlated with a lower overpotential for the HER. We discuss three possible reasons for the dependence of HER activity on proton insertion in tungsten oxides: 1) increase in electronic conductivity, 2) the influence of inserted protons on $\Delta G_{H,ads}$, and 3) participation of inserted protons in the HER mechanism.

II. RESULTS AND DISCUSSION

Synthesis and Characterization of $WO_3 \cdot H_2O$ and OA-WO_3

A series of interlayer-functionalized tungsten oxides were used to understand the role of electrochemical proton insertion on the HER in acidic electrolytes. Acid-precipitated $WO_3 \cdot 2H_2O$ was used as a precursor for the synthesis of the interlayer-functionalized tungsten oxides.[15] It was first dehydrated to obtain layered, orthorhombic $WO_3 \cdot H_2O$ **(Fig. 1a**). Stirring $WO_3 \cdot H_2O$ in octylamine and heptane leads to a dissolution-reorganization reaction and the formation of

layered OA-WO_3 (**Fig. 1b**).[16] Subsequent stirring of OA-WO_3 in an acidic solution leads to an exchange reaction with $WO_3 \cdot 2H_2O$ ($exWO_3 \cdot 2H_2O$) as the end-product.[14] SEM images in **Fig. 1d-f** show the morphology of each material. $WO_3 \cdot H_2O$ consists of nanoscale platelets typical of the acid-precipitated synthesis route. OA-WO_3 is composed of much larger micron-scale sheets and ribbons, consistent with a dissolution-reorganization reaction mechanism. $exWO_3 \cdot 2H_2O$ maintains a similar micron-scale sheet morphology, consistent with an exchange reaction. The surface area of each material was obtained by applying the Brunauer, Emmett, Teller (BET) technique to N_2 adsorption isotherms (**Fig. S1).** Surface area decreased in order of as-synthesized $WO_3 \cdot H_2O$ (31.0 m^2/g), OA-WO_3 (24.9 m^2/g), and $exWO_3 \cdot 2H_2O$ (16.4 m^2/g), following the morphology and particle size trend observed via SEM. The micron-scale, sheet-like morphology is maintained between OA-WO_3 and $exWO_3 \cdot 2H_2O$. This proved beneficial for the comparison of the HER activity of the two materials, since surface area and morphology can influence the electrocatalytic activity.

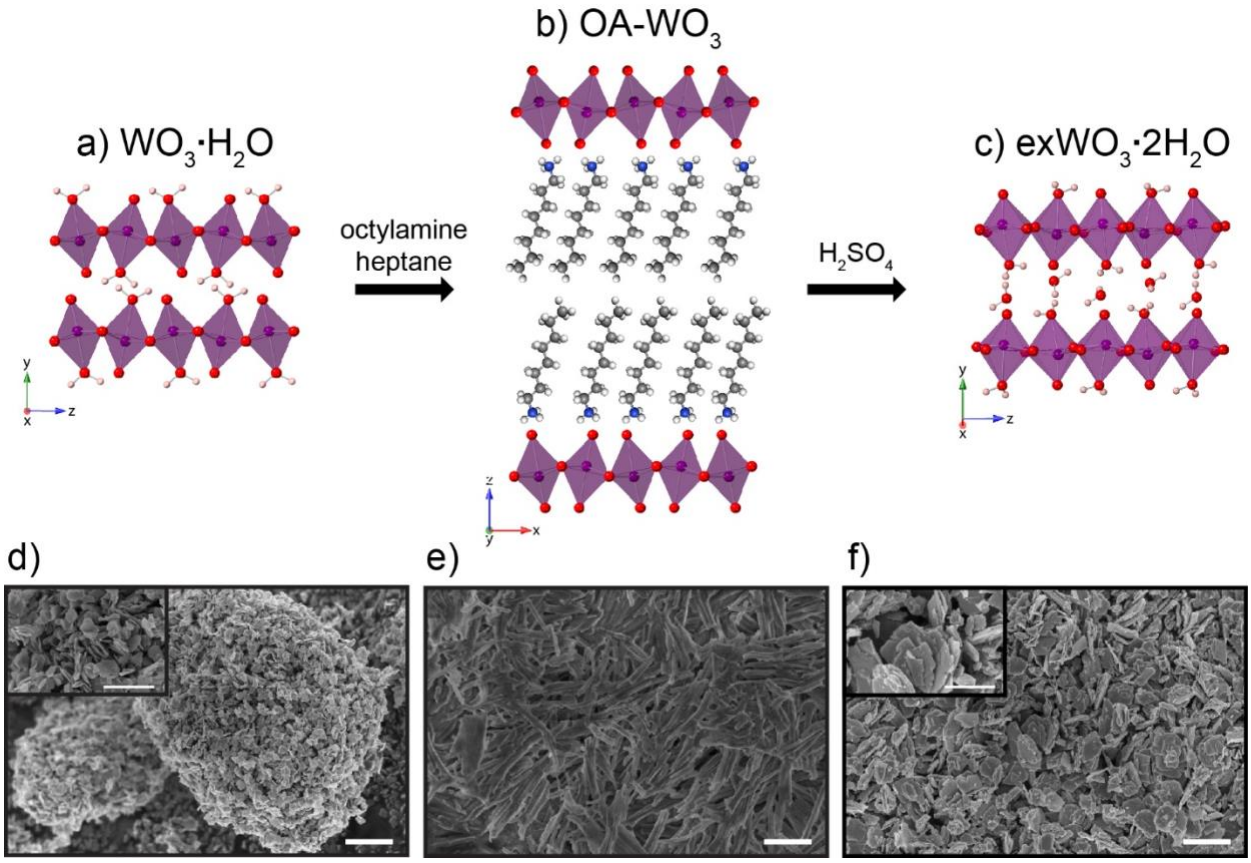

FIG. 1. Crystal structures of a) orthorhombic $WO_3 \cdot H_2O$, b) OA-WO_3 synthesized by a dissolution-reorganization reaction, and c) ex$WO_3 \cdot 2H_2O$ formed by acid-precipitation or exchange of protons with amines in OA-WO_3. Scanning electron micrographs of d) $WO_3 \cdot H_2O$, e) OA-WO_3, and f) ex$WO_3 \cdot 2H_2O$. Scale bars are 1 μm and 500 nm (insets).

X-ray diffraction (XRD) patterns (**Fig. 2**) show the formation of a molecularly pillared, layered structure after completion of the dissolution-reorganization reaction (OA-WO_3). The OA pillars increased the interlayer spacing from 0.53 nm in $WO_3 \cdot H_2O$ to 2.6 nm in OA-WO_3. Subsequent exchange of OA-WO_3 in 4 M H_2SO_4 (ex$WO_3 \cdot 2H_2O$) leads to the formation of $WO_3 \cdot 2H_2O$. The diffraction pattern of ex$WO_3 \cdot 2H_2O$ matched that of $WO_3 \cdot 2H_2O$ prepared via acid-precipitation, with both materials exhibiting an interlayer spacing of 0.69 nm.

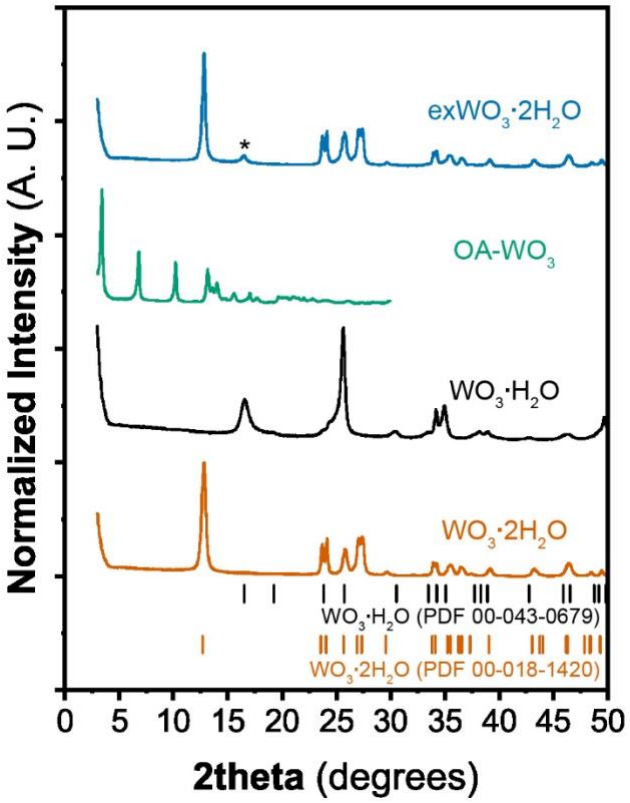

FIG. 2. XRD patterns of $WO_3 \cdot 2H_2O$ and $WO_3 \cdot H_2O$ formed by acid-precipitation, OA-WO_3, and $exWO_3 \cdot 2H_2O$. The largest interlayer spacing is observed in OA-WO_3 (2.6 nm) while $exWO_3 \cdot 2H_2O$ and $WO_3 \cdot 2H_2O$ exhibit the same crystal structure. * indicates the interlayer peak of $WO_3 \cdot H_2O$, a residual phase in $exWO_3 \cdot 2H_2O$. Powder diffraction file (PDF) 00-018-1420 corresponds to $WO_3 \cdot 2H_2O$; PDF 00-043-0679 corresponds to $WO_3 \cdot H_2O$.

We used Raman spectroscopy to distinguish differences in bonding between hydrated tungsten oxides ($WO_3 \cdot H_2O$ and $exWO_3 \cdot 2H_2O$) and OA-WO_3. **Fig. 3a** shows the spectra for $WO_3 \cdot H_2O$, OA-WO_3, and $exWO_3 \cdot 2H_2O$. The tungsten oxide hydrates each display two characteristic peaks. The broad peak between 550 and 750 cm^{-1} is assigned to the in-plane O-W-O stretching (ν) mode. $WO_3 \cdot H_2O$ and $exWO_3 \cdot 2H_2O$ contain a sharp peak at ~945 cm^{-1} and ~955 cm^{-1}, respectively, characteristic of the tungsten-to-terminal oxygen $\nu(W\text{-}O_t)$.[17] Replacing the coordinated water in the interlayer with the more basic (i.e., more electron-donating)

octylamine causes a shift of ν(W-O_t) to 885 cm^{-1}. Therefore, the resulting bond between the W center and terminal O is longer (i.e., weaker). **Table S1** presents the W-O_t bond lengths in $WO_3 \cdot H_2O$, $exWO_3 \cdot 2H_2O$, and OA-WO_3. OA-WO_3 also exhibits peaks at higher wavenumbers associated with octylamine. Peaks at 1430-1470 cm^{-1} are characteristic of CH_2 scissoring and bending modes, and those between 2830-2970 cm^{-1} are attributed to ν(C-H) from CH_2.

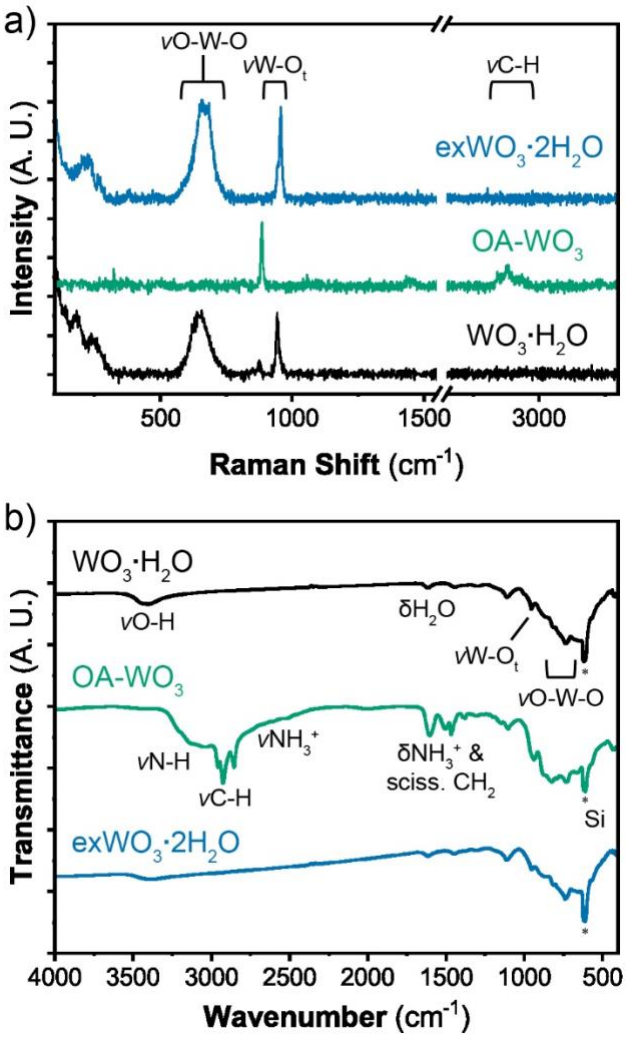

FIG. 3. The structure and chemical bonding within $WO_3 \cdot H_2O$, OA-WO_3, and $exWO_3 \cdot 2H_2O$ investigated via a) Raman spectroscopy and b) FTIR spectroscopy; ν indicates stretching, δ deformation/bending, and sciss. scissoring modes. * in the FTIR spectra indicates the Si substrate peak.

FTIR spectroscopy (**Fig. 3b**) corroborated the Raman results and provided further insight into the interlayer water and OA. The *v*(O-W-O) and *v*(W-O_t) vibrational modes were observed for WO_3·H_2O, OA-WO_3, and exWO_3·2H_2O. *v*(O-H) and H_2O deformation/bending (δ) modes located at ~3400 cm^{-1} and 1620 cm^{-1}, respectively, were observed in WO_3·H_2O and exWO_3·2H_2O. OA-WO_3 did not contain interlayer water, therefore corresponding O-H and H_2O peaks were not present. The presence of OA in OA-WO_3 was observed by the vibrational modes of NH_3^+ and CH_2.[18–20] Broad peaks at 3000-3250 cm^{-1} and 2500-3000 cm^{-1} were assigned to *v*(N-H) and asymmetrical and symmetrical *v*(NH_3^+), respectively. The δ(NH_3^+) was at 1606 cm^{-1} and the weak peak at ~1150 cm^{-1} was assigned to the *v*(C-N). *v*(C-H) from CH_2 in the alkyl chain was at 2957, 2925, and 2855 cm^{-1}. The peak at ~1504 cm^{-1} was attributed to CH_2 scissoring, and δ(CH_2) was observed at 1468 cm^{-1}.

XPS measurements of WO_3·H_2O, OA-WO_3, and exWO_3·*x*H_2O (**Fig. S2a-e**) were used to determine the surface chemical states of tungsten, oxygen, water, and OA. The survey spectrum of WO_3·H_2O shows the presence of W and O, as well as adventitious carbon (**Fig. S2a**). Based on XPS peak fitting of the W $4f_{5/2}$ and W $4f_{7/2}$ peaks, tungsten is in the 6+ oxidation state.[21,22] The O 1s core spectrum indicates the presence of O-W and O-H_2 bonds, consistent with the hydrated structure. The survey spectrum of OA-WO_3 shows the presence W, O, C, and N **(Fig. S2a**)**.** Peak fitting of the W 4f core spectrum showed that W is also in the 6+ oxidation state in OA-WO_3. The O 1s core spectrum for OA-WO_3 shows one peak at 530.8 eV that corresponds to O-W binding. Two peaks were present in the N 1s core spectrum. The peak at 399.7 eV was attributed to OA in the form of an alkylamine (R-NH_2), and the peak at 401.6 eV was attributed to OA in the form of an alkylammonium (R-NH_3^+).[23] Thermogravimetric analysis (TGA) (**Fig. S3**) shows that there are approximately 2.6 moles of OA to 1 mole of WO_3 in OA-WO_3. Given that XPS shows tungsten is in the 6+ oxidations state, we hypothesize that most of the OA pillars are alkylammonium cations to compensate for the negative charge of the WO_4^{2-} inorganic layer. The survey scan of

exWO_3·2H_2O showed that it contains W and O (**Fig. S2a**), and peak fitting of the W 4f and O 1s core spectra revealed the same chemical states as in WO_3·H_2O.

Electrochemical cation insertion in OA-WO_3 and WO_3·*x*H_2O

We first investigated the role of interlayer pillaring molecules on electrochemical cation insertion into tungsten oxides. We performed cyclic voltammetry in three different electrolytes to determine the insertion behavior of three cations: 1 M H_2SO_4 (H^+), 1 M $LiClO_4$ in PC (Li^+), and 0.1 M TBAP in PC (TBA^+). Electrochemical insertion of small monovalent cations (A = H^+, Li^+) into WO_3 and its hydrates occurs up to *n* = 1:[13]

$$WO_3{\cdot}xH_2O + nA^+ + ne^- \leftrightarrow A_nWO_3{\cdot}xH_2O \quad (1)$$

Fig. 4a shows the cyclic voltammograms (CVs; cycle 3) of WO_3·H_2O and OA-WO_3 in 1 M H_2SO_4 at 10 mV s^{-1}. Proton insertion into WO_3·H_2O is reversible, with nearly symmetrical current response and an anodic capacity of 20 mAh g^{-1} (0.19 e^-/W). Reversibility here refers to electrochemical proton insertion during cathodic polarization and proton de-insertion during anodic polarization (e.g. the Coulombic efficiency). Conversely, proton insertion is largely suppressed in OA-WO_3, with a capacity of only 1 mAh g^{-1} (0.02 e^-/W). Our prior results showed that proton insertion in WO_3·H_2O is favored at bridging oxygen sites within the corner-sharing $WO_5(OH_2)$ network.[13] The lack of proton insertion in OA-WO_3 suggests that access to these bridging sites is blocked by the OA.

Fig. 4b shows a similar outcome for Li^+ insertion. There is virtually no Li^+ insertion in OA-WO_3 (0.008 e^-/W), while WO_3·H_2O has the same capacity for Li^+ as for H^+ (20 mAh g^{-1}; 0.19 e^-/W). **Fig. 4c** shows that TBA^+ insertion is restricted for both materials: the observed capacities for WO_3·H_2O and OA-WO_3 were 0.53 mAh g^{-1} (0.005 e^-/W) and 0.21 mAh g^{-1} (0.004 e^-/W), respectively. This suggests that charge storage is only due to surface adsorption processes. The restricted insertion of TBA^+ in WO_3·H_2O is likely due to steric hindrance from the inorganic layers, since its ionic diameter (0.83 nm)[24] is larger than the interlayer spacing of 0.53 nm. However, the

interlayer spacing of OA-WO_3 (2.6 nm) should provide sufficient space for TBA^+ insertion. An alternative explanation, in agreement with similar studies,[25] is that the interlayer OA pillar density is too high to allow insertion of guest cations. **Fig. 4d** summarizes the electrons stored per tungsten in each electrode when cycled in electrolytes containing three different size cations. These results indicate that the presence of interlayer OA molecules in tungsten oxides suppresses proton and cation insertion, whereas the presence of interlayer H_2O molecules does not restrict the insertion of small cations like H^+ and Li^+.

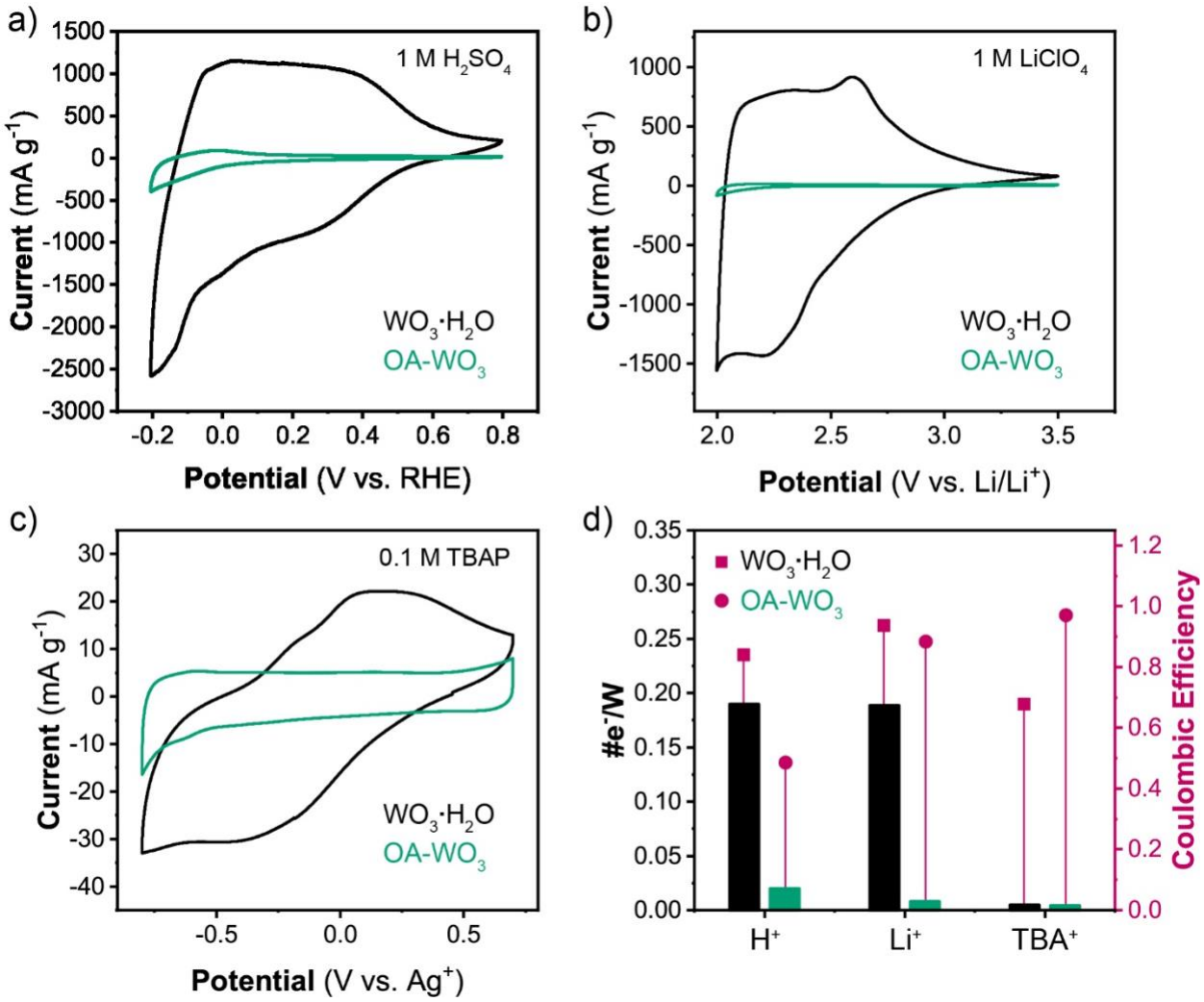

FIG. 4. Cyclic voltammetry of $WO_3{\cdot}H_2O$ and OA-WO_3 at 10 mV s^{-1} in electrolytes with three different size cations: a) 1 M H_2SO_4, b) 1 M $LiClO_4$ in PC, and c) 0.1 M TBAP in PC. d) The number

of electrons per tungsten (bars) and Coulombic efficiency (data points) for $WO_3 \cdot H_2O$ and OA-WO_3 in each electrolyte.

Continued electrochemical cycling of OA-WO_3 in 1 M H_2SO_4 led to an increase in capacity with cycle number. **Fig. 5a** shows CVs of OA-WO_3 cycled 250 times in 1 M H_2SO_4 at 10 mV s^{-1}. The CV characteristics of the 250th cycle (symmetrical CV shape, insertion current over a broad potential range, and redox peaks centered at 0.27 V) are like those associated with proton insertion into $WO_3 \cdot 2H_2O$. The capacity of OA-WO_3 increased from 0.02 to 0.18 e^-/W from cycle 1 to cycle 250. Ex situ XRD (**Fig. 5b**) after 50 and 200 cyclic voltammetry cycles showed the disappearance of the (001) peak of OA-WO_3 at 3.9° 2θ, and the emergence of a peak at 12.8° 2θ consistent with the (010) peak of $WO_3 \cdot 2H_2O$. These structural changes indicate an electrochemically-assisted transformation of OA-WO_3 to $WO_3 \cdot 2H_2O$ in the acidic electrolyte, similar to the chemical exchange process to obtain ex$WO_3 \cdot 2H_2O$.

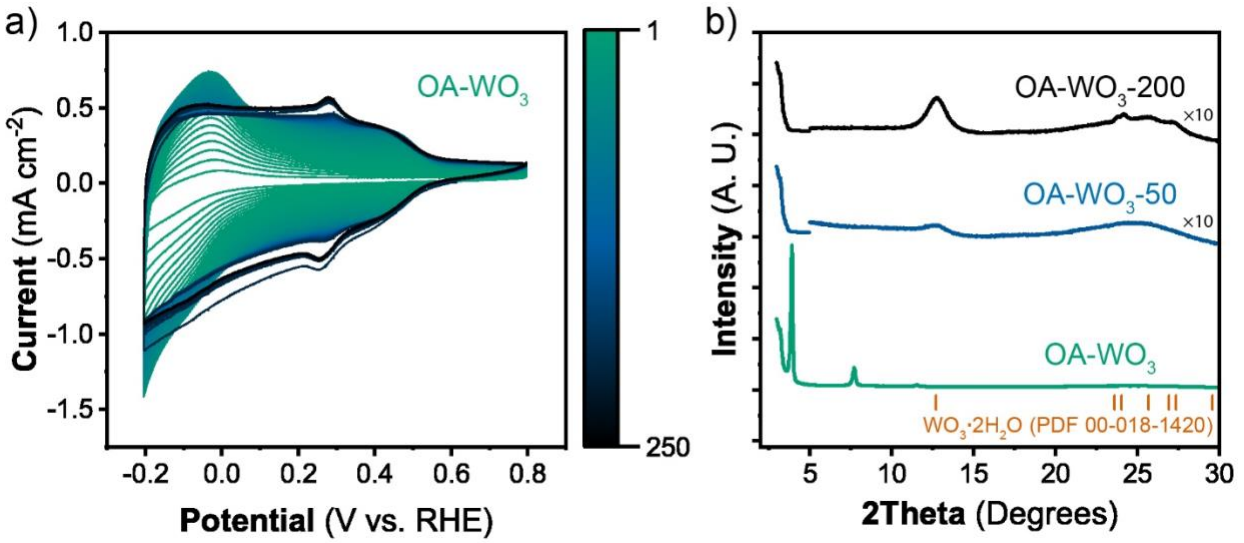

FIG. 5. a) Cyclic voltammetry of OA-WO_3 in 1 M H_2SO_4 for 200 cycles at 10 mV s^{-1} showing the transition from OA-WO_3 to a tungsten oxide hydrate indicated by increased proton insertion current, and b) ex situ XRD showing the structural transformation of OA-WO_3 to $WO_3 \cdot 2H_2O$ after

200 cycles. The transformation is already apparent within 50 cycles. The intensity of cycled OA-WO_3 at 2Theta > 5° was multiplied by 10 to aid in the visualization of higher angle diffraction peaks.

Overpotential for HER decreases with increasing proton insertion capacity

Cyclic voltammetry was used to investigate the role of proton insertion on the HER activity of tungsten oxides by comparing OA-WO_3, OA-WO_3-200, exWO_3·2H_2O, WO_3·H_2O, and WO_3·2H_2O (**Fig. 6**). The reasons for comparing the behavior of these five materials are the following: The lack of proton insertion in OA-WO_3 and its transformation to the proton-inserting WO_3·2H_2O in acidic electrolyte provides a materials platform to understand the role of proton insertion on the HER activity of transition metal oxides. The HER activity of OA-WO_3 was compared to OA-WO_3 that underwent 200 electrochemical cycles (OA-WO_3-200) and chemically-exchanged exWO_3·2H_2O. OA-WO_3-200 provides the same electrode film structure and similar surface area, with the main differences being the replacement of OA with interlayer water and the inherent decrease in interlayer spacing. exWO_3·2H_2O shares the same characteristics as OA-WO_3-200, but has better electrochemical cycling stability since the OA/H_2O exchange occurred prior to electrode fabrication. As-synthesized WO_3·H_2O and WO_3·2H_2O exhibit reversible proton insertion and have the same surface area and morphology. Finally, exWO_3·2H_2O and OA-WO_3-200 were compared to as-synthesized WO_3·H_2O and WO_3·2H_2O to determine whether hydrated materials obtained from exchange with OA retained the same electrochemical insertion and HER characteristics.

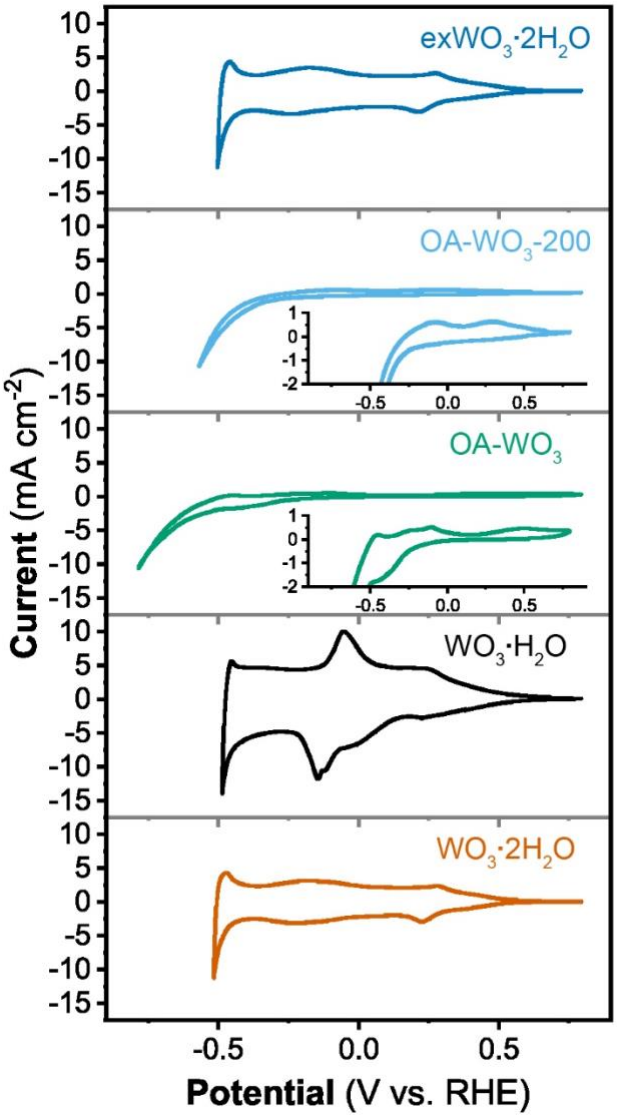

FIG. 6. Cyclic voltammetry at 10 mV s^{-1} to determine the relationship between proton insertion and HER current in OA-WO_3, OA-WO_3-200, exWO_3·2H_2O, WO_3·H_2O, and WO_3·2H_2O. The cathodic potential limit was the potential where the current was ~ -10 mA cm^{-2} (-14 mA cm^{-2} for WO_3·H_2O due to the magnitude of the insertion peaks).

The hydrated materials (WO_3·2H_2O, WO_3·H_2O, and exWO_3·2H_2O) show similar CV shapes, with proton insertion over a broad potential range before the onset of the HER. WO_3·2H_2O and exWO_3·2H_2O have two similar redox peaks centered at -0.2 and 0.25 V vs. RHE. WO_3·H_2O has one distinct set of redox peaks at -0.1 V as well as broad, symmetric peaks between 0 and

0.25 V. These peaks are associated with structural transformations due to proton insertion.[13] Ex situ Raman spectroscopy (**Fig. S4**) shows that all three of the hydrated materials return to their original structure after cycling, indicating reversibility of the proton insertion process. OA-WO_3 cycled 200 times between -0.2 V and 0.8 V showed anodic peaks similar to the tungsten oxide hydrates. This is expected based on its transformation to the $WO_3 \cdot 2H_2O$ structure, corroborated by ex situ Raman spectra in **Fig. S4**. The O-W-O and W-O_t stretching modes aligned with the positions expected for $WO_3 \cdot 2H_2O$. The anodic capacity of ~0.13 e^-/W is lower than expected, however, this may be underestimated due to possible loss of active material and electrical contact from volume change upon exchange of OA with water. OA-WO_3 undergoes an irreversible reduction event at approximately -0.45 V vs. RHE, close to the onset of the HER. Ex situ Raman spectroscopy (**Figure S4**) after 5 cyclic voltammetry cycles revealed a new peak at ~960 cm^{-1} (shifted to higher wavenumbers compared to the expected peaks for $WO_3 \cdot xH_2O$). The shifted W-O_t peak and lack of a broad peak associated with O-W-O stretching modes show that OA-WO_3 does not transform to a tungsten oxide hydrate. Furthermore, ex situ XRD showed no long-range order for OA-WO_3 cycled five times to an average cutoff potential of 0.764 V vs. RHE (**Figure S5**). The peak around 3.9° 2θ disappeared, and there was no evidence of crystalline hydrates. This result confirms that the reduction event at -0.45 V vs. RHE causes an irreversible structural transformation in OA-WO_3. Although the structure is distorted during cycling, the electrocatalytic activity remains consistent and distinct from the hydrates. These results demonstrate that for all five materials, the HER does not occur without proton insertion. In particular, blocking of proton insertion (OA-WO_3) leads to the lowest HER activity.

To better highlight the different HER activity of the five materials, we subtracted the capacitive and proton insertion current from the CVs (method described in Supplementary Material **Fig. S6**); the residual current, attributed to the HER, is shown in **Fig. 7a**. We compared the HER activity by determining the onset of the HER, defined as the overpotential (η) at 5 mA cm^{-2} based on the geometric surface area. $WO_3 \cdot H_2O$ had the lowest η value, 470 mV. $WO_3 \cdot 2H_2O$

and $exWO_3 \cdot 2H_2O$ showed slightly higher η of 502 mV and 485 mV, respectively. OA-WO_3 cycled 200 times between -0.2 V and 0.8 V showed an η of 478 mV, similar to the tungsten oxide hydrates. OA-WO_3 shows the lowest HER activity with an η of 682 mV.

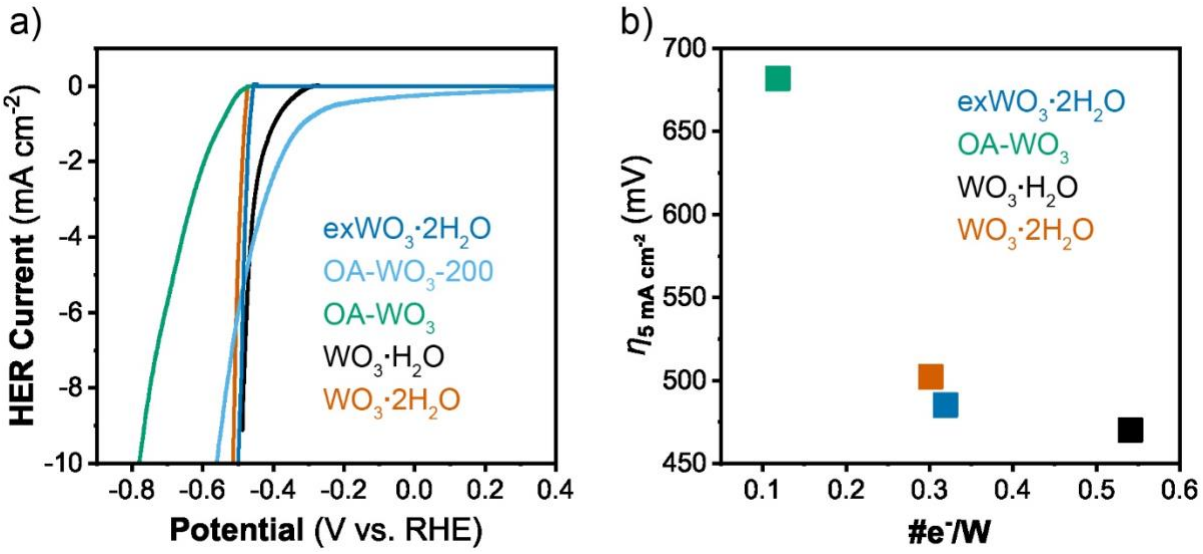

FIG. 7. a) Residual cathodic current (attributed to the HER) after subtraction of the capacitive and insertion current contributions at 10 mV s^{-1}, and b) the overpotential for the HER (determined from Fig. 7a) vs. #e^- stored in the material (calculated from the anodic scan of the CVs).

The decrease of HER activity with OA-WO_3 compared to tungsten oxide hydrates could arise from different mechanisms: (1) low electrochemically-active surface area, (2) blocking of the electrochemical interface by OA molecules, or (3) the lack of proton insertion in OA-WO_3 which is necessary to "activate" the material for the HER. The fact that OA-WO_3 has a surface area and morphology similar to $exWO_3 \cdot 2H_2O$ and OA-WO_3-200 but lower HER activity makes mechanism (1) unlikely. With respect to mechanism (2), Malkhandi et al. reported that alkyl chains attached to the surface of an Fe electrode suppressed the HER by hindering electron transfer and decreasing the accessible surface area.[26] Although the outer surfaces of OA-WO_3 are likely coated with OA, we observed that long-term soaking or stirring of OA-WO_3 in acidic conditions

leads to $WO_3 \cdot 2H_2O$. We performed in situ Raman spectroscopy to determine how quickly this reaction occurs to expose electrochemically active surface sites in acidic electrolyte (**Fig. S7**). Within 2.5 minutes, a peak emerged at ~955 cm^{-1} characteristic of $WO_3 \cdot 2H_2O$. This rapid transformation of the near-surface structure indicates that surface and near-surface interlayer OA molecules do not hinder the accessible surface area or electron transfer. Furthermore, the lack of polarization observed in the CVs in **Fig. 5a** along with some proton insertion into the structure suggests that electron transport in the hybrid material is not limiting the electrocatalytic activity. Therefore, we expect that OA-WO_3 has sufficient electronic conductivity and a suitable surface composition in acidic conditions to catalyze the HER making mechanism (2) an unlikely reason for its low activity compared to the tungsten oxide hydrates.

With respect to mechanism (3), **Fig. 4a** and **Fig. 6** show that the electrochemical response due to proton insertion differs significantly between OA-WO_3 and tungsten oxide hydrates. Each material displays at least one reduction reaction associated with proton insertion, however, the reduction peak positions and proton storage capacities differ considerably between the materials. **Fig. 7b** shows the relationship between η and the number of electrons/protons inserted per tungsten (calculated from the anodic current response) for OA-WO_3 and the tungsten oxide hydrates. More proton insertion decreases the overpotential for the HER. The relationship between insertion capacity and overpotential demonstrates that the HER is dependent on the electrochemical insertion characteristics in transition metal oxides.

There are several hypotheses for why proton insertion in $WO_3 \cdot xH_2O$ contributes to improved HER activity: 1) proton insertion changes the electronic band structure of $WO_3 \cdot xH_2O$, 2) the presence of bulk protons can influence $\Delta G_{H,ads}$ at the surface sites, and 3) inserted protons may participate in the HER mechanism on $WO_3 \cdot xH_2O$. With respect to mechanism (1), proton insertion in tungsten oxides causes a semiconductor-to-metallic transition.[14,27] Electrons filling the conduction band states increase the electrical conductivity and may facilitate proton-coupled electron transfer during the HER. Additionally, $WO_3 \cdot H_2O$ accommodates 0.24 more

protons/electrons per W than $WO_3 \cdot 2H_2O$ and η is 32 mV lower (**Fig. 7b**). This suggests that higher proton insertion capacity and thus higher filling of conduction band states enhances HER activity. Mechanism (2) must also be considered as a possibility, as $\Delta G_{H,ads}$ is one of the most common descriptors of a material's activity toward the HER. Protons generally prefer to bind to more basic sites, and Miu et al. recently reported that hydrogen adsorption and proton insertion potentials are dependent on the proton concentration in H_xWO_3.[28] In this work, the material with a higher proton insertion capacity shows the lowest overpotential for the HER. Given that the HER is most active on surfaces with a $\Delta G_{H,ads}$ close to 0 eV, one could hypothesize that as the proton concentration in $H_xWO_3 \cdot xH_2O$ increases, $\Delta G_{H,ads}$ approaches 0 eV and reduces the overpotential required to catalyze the HER. Mechanism (3), whereby adsorption and insertion of protons are coupled, suggests that inserted protons can also migrate to the surface to participate in the HER. Proton insertion into $WO_3 \cdot xH_2O$ begins at 0.5 V vs. RHE, thus protons are present in the material prior to reaching the thermodynamic driving force required for the HER. We hypothesize that the high mobility of protons in $WO_3 \cdot xH_2O$ could enable transport to the surface to participate in the HER. Based on this mechanism, the HER activity could be partially dependent on the transport kinetics of the inserted protons to electrocatalytically active sites, in addition to other factors such as electronic conductivity and $\Delta G_{H,ads}$.

III. CONCLUSIONS

In this work, we used a materials chemistry approach to understand the role of proton insertion in transition metal oxides on HER catalysis. We synthesized tungsten oxide hydrates and a molecularly-pillared tungsten oxide (OA-WO_3) that exhibit different capacities for proton and cation insertion. We observed broad proton insertion peaks across a wide range of potentials in the tungsten oxide hydrates, while proton insertion did not occur until -0.45 V in OA-WO_3. The proton insertion capacity of OA-WO_3 (~0.12 H^+/W) was considerably lower than that of $WO_3 \cdot 2H_2O$

(0.3 H^+/W) and $WO_3 \cdot H_2O$ (0.54 H^+/W). Lower proton insertion was correlated with a higher overpotential for the HER: 682 mV for OA-WO_3, whereas $WO_3 \cdot 2H_2O$ and $WO_3 \cdot H_2O$ only required 502 mV and 470 mV, respectively. These results indicate that the HER activity of a transition metal oxide is dependent on the proton insertion capacity. We propose three possible mechanisms to explain this trend: 1) proton insertion changes the electronic band structure, 2) the presence of bulk protons can influence the $\Delta G_{H,ads}$ at the surface sites, and 3) inserted protons may participate in the HER mechanism on $WO_3 \cdot xH_2O$. Future work includes determining whether this trend also occurs for anhydrous WO_3, the most likely mechanism, and whether it is a general phenomenon occurring at transition metal oxides undergoing the HER in acidic electrolytes.

IV. EXPERIMENTAL SECTION

A. Materials Synthesis

$WO_3 \cdot H_2O$ was synthesized via an acid-precipitation reaction.[15] Briefly, 50 mL of 1 M $Na_2WO_4 \cdot 2H_2O$ (99+% Acros Organics) was added dropwise to 450 mL of 4 N HCl (Certified ACS Plus, Fisher Chemical) while stirring at 300 rpm for approximately 24 hours. The precipitates were collected and washed with deionized water using vacuum filtration until the rinse solution reached pH 6-7. The filtered $WO_3 \cdot 2H_2O$ was then dried at 60°C overnight and ground into a fine powder. To obtain $WO_3 \cdot H_2O$, the $WO_3 \cdot 2H_2O$ powder was heated overnight at 120°C.

OA-WO_3 was synthesized by a dissolution-reorganization reaction using $WO_3 \cdot H_2O$ as the precursor.[16] $WO_3 \cdot H_2O$ was added to a solution of OA (99+%, Acros Organics) in heptane (99%, Acros Organics) with a molar ratio of 15 OA to 1 $WO_3 \cdot H_2O$, and a volume ratio of 5 heptane to 1 octylamine independent of the size of the reaction. This mixture was stirred rigorously in a round-bottom flask for six days. The reaction completion was marked by a color change from yellow to white. After completion, the powder was collected via centrifugation and washed by redispersing the powder in ethanol and centrifuging three times. The resulting material was dried at 60°C under vacuum and ground to form a fine powder.

Exchanged $WO_3 \cdot 2H_2O$ ($exWO_3 \cdot 2H_2O$) was obtained by stirring OA-WO_3 in 4 M H_2SO_4 (Certified ACS Plus, Fisher Chemical). The sulfuric acid was refreshed daily by centrifuging the powder and re-dispersing in a new solution until the powder turned yellow. $exWO_3 \cdot 2H_2O$ was collected via the same centrifugation procedure as OA-WO_3. The resulting material was dried at 60°C overnight and ground to a fine powder.

B. Physical characterization

SEM was performed using a field emission FEI Verios 460L microscope. Raman spectroscopy was performed using a WiTEC alpha 300R confocal Raman spectrometer with a laser wavelength of 532 nm and a 100x objective lens. FTIR spectroscopy was performed on a Thermo Scientific Nicolet 6700 spectrometer with the chamber purged with dry air. Spectra were collected in transmission mode with 200 scans between 4000 and 400 cm^{-1}. XPS was conducted with a SPECS FlexMod XPS instrument with Mg Ka excitation (1254 eV) and a hemispherical analyzer (PHOIBIS 150). The takeoff angle was normal to the surface. Charge neutralization was used for $WO_3 \cdot H_2O$ and $exWO_3 \cdot 2H_2O$. Spectra were calibrated to the C 1s peak of adventitious carbon at 285.0 eV. Peak fitting of XPS spectra was performed with CasaXPS software and all spectra were fitted with a Shirley background. TGA was performed on a Seiko Exstar TG/DTA6200 instrument. XRD measurements were conducted on a PANalytical Empyrean diffractometer in the Bragg-Brentano geometry with Cu Ka radiation (λ = 1.54 Å). Ex situ XRD was completed using slurry electrodes coated on glassy carbon substrates.

C. Electrode preparation

All electrodes for electrochemistry in acidic electrolytes were prepared by mixing the active material with acetylene black and a 5 wt% solution of Nafion in ethanol. The masses of active material, acetylene black, and Nafion were controlled to obtain a 60:10:30 weight ratio, respectively. Electrodes of the tungsten oxide hydrates for non-aqueous electrochemistry were

prepared by mixing $WO_3 \cdot xH_2O$ in ethanol and casting 400 µg of material onto glassy carbon substrates. Slurries of OA-WO_3 were prepared by mixing 80 wt% OA-WO_3, 10 wt% acetylene black, and 10 wt% Latex-PVDF using a 20 wt% Latex-PVDF aqueous dispersion. Slurries were cast on glassy carbon plates or glassy carbon disk electrodes. Glassy carbon plates (2x1 cm) were prepared by sonication in detergent, rinsing with DI H_2O, sonicating in ethanol, and rinsing with DI H_2O. The substrates were dried at 60°C and Kapton tape was used to expose only the slurry-coated area to the electrolyte. The glassy carbon substrates were plasma cleaned immediately before drop-casting (Harrick Plasma PDC-32G). Disk electrodes were polished with 0.05 µm alumina slurries followed by rinsing and sonication in DI H_2O and ethanol.

D. Electrochemical characterization

Electrochemical characterization was conducted in three-electrode cells using a potentiostat (Bio-Logic MPG2 and VMP3). All cyclic voltammetry measurements used a scan rate of 10 mV s^{-1}. Proton insertion and hydrogen evolution reactions were carried out in 1 M H_2SO_4 (Certified ACS Plus, Fisher Chemical) with the working electrode (vide supra), a graphite rod counter electrode (Pine Research Instrumentation; unless specified otherwise), and a Ag/AgCl in 4 M KCl reference electrode (Pine Research Instrumentation). See Supplementary Material **Fig. S8** for electrochemical cycling of OA-WO_3 with a Pt counter electrode and comparison of Coulombic efficiency when using a graphite vs. Pt counter electrode. The overpotential for HER was defined as the potential vs. RHE at which the current reached 5 mA cm^{-2}, and all reported current densities were based on the geometric surface area. Potentials were converted to the reversible hydrogen electrode (RHE) scale using **Equation 2**:

$$E_{RHE} = E_{meas} + E_{Ag/AgCl} + 0.059pH \quad (2)$$

Non-aqueous electrochemistry was performed in an argon-filled glovebox (MBraun, <1 ppm O_2, H_2O). Li^+ insertion was studied in a 1 M $LiClO_4$ (electrochemical grade, Sigma-Aldrich) in PC

(Sigma-Aldrich) electrolyte with the working electrode (vide supra) and Li metal counter and reference electrodes (99.9%, Sigma-Aldrich). TBA^+ insertion was studied in a 0.1 M TBAP (Sigma-Aldrich) in PC electrolyte with a working electrode (vide supra), a Pt coil counter electrode (99.99%, Pine Research Instrumentation), and a Ag pseudoreference electrode.

V. SUPPLEMENTARY MATERIAL

See supplementary material for N_2 adsorption isotherms, W-O_t bond lengths, XPS & TGA results, ex situ Raman & XRD of OA-WO_3 after HER testing, discussion of irreversible transformation in OA-WO_3 during HER testing, CVs showing the capacitive and insertion current subtraction, in situ Raman spectra of OA-WO_3 in H_2SO_4, and CVs & Coulombic efficiency of OA-WO_3 cycled with graphite and Pt counter electrodes.

VI. ACKNOWLEDGEMENTS

The authors would like to thank Dr. Fred Stevie for assisting with XPS measurements and Sarah Morgan for acquiring N_2 adsorption isotherms. This material is based upon work supported by the U.S. Department of Energy, Office of Science, Office of Basic Energy Sciences, Early Career Research Program under Award Number DE-SC0020234. This work was performed in part at the Analytical Instrumentation Facility (AIF) at North Carolina State University, which is supported by the State of North Carolina and the National Science Foundation (award # ECCS-2025064). The AIF is a member of the North Carolina Research Triangle Nanotechnology Network (RTNN), a site in the National Nanotechnology Coordinated Infrastructure (NNCI).

VII. DATA AVAILABILITY

The data that support the findings of this study are openly available in Materials Cloud at http://doi.org/10.24435/materialscloud:1k-tm, reference number 29.

VIII. REFERENCES

[1] A. Elgowainy, M. Mintz, U. Lee, T. Stephens, P. Sun, K. Reddi, Y. Zhou, G. Zang, M. Ruth, P. Jadun, E. Connelly, and R. Boardman, *Assessment of Potential Future Demands for Hydrogen in the United States* (2020).

[2] L. Wu and J.P. Hofmann, "Comparing the Intrinsic HER Activity of Transition Metal Dichalcogenides: Pitfalls and Suggestions," ACS Energy Lett. **6**, 2619 (2021). https://doi.org/10.1021/acsenergylett.1c00912

[3]*Department of Energy Hydrogen Program Plan* (2020).

[4] Y. Zhu, Q. Lin, Y. Zhong, H.A. Tahini, Z. Shao, and H. Wang, "Metal oxide-based materials as an emerging family of hydrogen evolution electrocatalysts," Energy Environ. Sci. **13**, 3361 (2020). https://doi.org/10.1039/D0EE02485F

[5] T.F. Jaramillo, K.P. Jørgensen, J. Bonde, J.H. Nielsen, S. Horch, and I. Chorkendorff, "Identification of Active Edge Sites for Electrochemical H_2 Evolution from MoS_2 Nanocatalysts," Science **317**, 100 (2007). https://doi.org/10.1126/science.1141483

[6] Y. Shi and B. Zhang, "Recent advances in transition metal phosphide nanomaterials: synthesis and applications in hydrogen evolution reaction," Chem. Soc. Rev. **45**, 1529 (2016). https://doi.org/10.1039/C5CS00434A

[7] Z.W. Seh, J. Kibsgaard, C.F. Dickens, I. Chorkendorff, J.K. Nørskov, and T.F. Jaramillo, "Combining theory and experiment in electrocatalysis: Insights into materials design," Science **355**, (2017). https://doi.org/10.1126/science.aad4998

[8] J.T. Mefford, A.R. Akbashev, M. Kang, C.L. Bentley, W.E. Gent, H.D. Deng, D.H. Alsem, Y.-S. Yu, N.J. Salmon, D.A. Shapiro, P.R. Unwin, and W.C. Chueh, "Correlative operando microscopy of oxygen evolution electrocatalysts," Nature **593**, 67 (2021). https://doi.org/10.1038/s41586-021-03454-x

[9] M. Su, W. Zhou, Z. Jiang, M. Chen, X. Luo, J. He, and C. Yuan, "Elimination of Interlayer Potential Barriers of Chromium Sulfide by Self-Intercalation for Enhanced Hydrogen Evolution

Reaction," ACS Appl. Mater. Interfaces **13**, 13055 (2021). https://doi.org/10.1021/acsami.0c20577

[10] S. Parvin, V. Hazra, A.G. Francis, S.K. Pati, and S. Bhattacharyya, "In Situ Cation Intercalation in the Interlayer of Tungsten Sulfide with Overlaying Layered Double Hydroxide in a 2D Heterostructure for Facile Electrochemical Redox Activity," Inorg. Chem. **60**, 6911 (2021). https://doi.org/10.1021/acs.inorgchem.1c00011

[11] N.H. Attanayake, A.C. Thenuwara, A. Patra, Y. V. Aulin, T.M. Tran, H. Chakraborty, E. Borguet, M.L. Klein, J.P. Perdew, and D.R. Strongin, "Effect of Intercalated Metals on the Electrocatalytic Activity of 1T-MoS_2 for the Hydrogen Evolution Reaction," ACS Energy Lett. **3**, 7 (2018). https://doi.org/10.1021/acsenergylett.7b00865

[12] R. Gao, G. Yu, W. Chen, G.-D. Li, S. Gao, Z. Zhang, X. Shen, X. Huang, and X. Zou, "Host–Guest Interaction Creates Hydrogen-Evolution Electrocatalytic Active Sites in 3d Transition Metal-Intercalated Titanates," ACS Appl. Mater. Interfaces **10**, 696 (2018). https://doi.org/10.1021/acsami.7b15617

[13] J.B. Mitchell, N.R. Geise, A.R. Paterson, N.C. Osti, Y. Sun, S. Fleischmann, R. Zhang, L.A. Madsen, M.F. Toney, D. Jiang, A.I. Kolesnikov, E. Mamontov, and V. Augustyn, "Confined Interlayer Water Promotes Structural Stability for High-Rate Electrochemical Proton Intercalation in Tungsten Oxide Hydrates," ACS Energy Lett. **4**, 2805 (2019). https://doi.org/10.1021/acsenergylett.9b02040

[14] J.B. Mitchell, W.C. Lo, A. Genc, J. LeBeau, and V. Augustyn, "Transition from Battery to Pseudocapacitor Behavior via Structural Water in Tungsten Oxide," Chem. Mater. **29**, 3928 (2017). https://doi.org/10.1021/acs.chemmater.6b05485

[15] M.L. Freedman, "The Tungstic Acids," J. Am. Chem. Soc. **81**, 3834 (1959). https://doi.org/10.1021/ja01524a009

[16] D. Chen, T. Li, L. Yin, X. Hou, X. Yu, Y. Zhang, B. Fan, H. Wang, X. Li, R. Zhang, T. Hou, H. Lu, H. Xu, J. Sun, and L. Gao, "A comparative study on reactions of n-alkylamines with tungstic

acids with various W–O octahedral layers: Novel evidence for the “dissolution–reorganization” mechanism," Mater. Chem. Phys. **125**, 838 (2011). https://doi.org/10.1016/j.matchemphys.2010.09.039

[17] M.F. Daniel, B. Desbat, J.C. Lassegues, B. Gerand, and M. Figlarz, "Infrared and Raman study of WO_3 tungsten trioxides and WO_3*xH_2O tungsten trioxide hydrates," J. Solid State Chem. **67**, 235 (1987). https://doi.org/10.1016/0022-4596(87)90359-8

[18] R.M. Silverstein, G.C. Bassler, and T.C. Morrill, *Spectrometric Identification of Organic Compounds*, 5th ed. (John Wiley & Sons, Inc, New York, 1991).

[19] B. Ingham, S. V. Chong, and J.L. Tallon, "Layered Tungsten Oxide-Based Organic−Inorganic Hybrid Materials: An Infrared and Raman Study," J. Phys. Chem. B **109**, 4936 (2005). https://doi.org/10.1021/jp045066l

[20] B. Ingham, Low-Dimensional Physics of Organic-Inorganic Multilayers, Victoria University of Wellington, (2005).

[21] O.Y. Khyzhun, "XPS, XES and XAS studies of the electronic structure of tungsten oxides," J. Alloys Compd. **305**, 1 (2000). https://doi.org/10.1016/S0925-8388(00)00697-6

[22] Islah-u-din, S. V. Chong, S.G. Telfer, J. Kennedy, G.B. Jameson, M.R. Waterland, and J.L. Tallon, "Influence of Doping on Hybrid Organic–Inorganic WO_3(4,4′-bipyridyl)$_{0.5}$ Materials," J. Phys. Chem. C **116**, 3787 (2012). https://doi.org/10.1021/jp2115324

[23] W. Li, F. Xia, J. Qu, P. Li, D. Chen, Z. Chen, Y. Yu, Y. Lu, R.A. Caruso, and W. Song, "Versatile inorganic-organic hybrid WO_x-ethylenediamine nanowires: Synthesis, mechanism and application in heavy metal ion adsorption and catalysis," Nano Res. **7**, 903 (2014). https://doi.org/10.1007/s12274-014-0452-9

[24] M. Ue, "Mobility and Ionic Association of Lithium and Quaternary Ammonium Salts in Propylene Carbonate and γ-Butyrolactone," J. Electrochem. Soc. **141**, 3336 (1994). https://doi.org/10.1149/1.2059336

[25] H. Banda, S. Périé, B. Daffos, P.-L. Taberna, L. Dubois, O. Crosnier, P. Simon, D. Lee, G. De

Paëpe, and F. Duclairoir, "Sparsely Pillared Graphene Materials for High-Performance Supercapacitors: Improving Ion Transport and Storage Capacity," ACS Nano **13**, 1443 (2019). https://doi.org/10.1021/acsnano.8b07102

[26] S. Malkhandi, B. Yang, A.K. Manohar, G.K.S. Prakash, and S.R. Narayanan, "Self-Assembled Monolayers of n -Alkanethiols Suppress Hydrogen Evolution and Increase the Efficiency of Rechargeable Iron Battery Electrodes," J. Am. Chem. Soc. **135**, 347 (2013). https://doi.org/10.1021/ja3095119

[27] H.R. Shanks, P.H. Sidles, and G.C. Danielson, "Electrical Properties of the Tungsten Bronzes," Adv. Chem. **39**, 237−245 (1963).

[28] E. V. Miu, G. Mpourmpakis, and J.R. McKone, "Predicting the Energetics of Hydrogen Intercalation in Metal Oxides Using Acid–Base Properties," ACS Appl. Mater. Interfaces **12**, 44658 (2020). https://doi.org/10.1021/acsami.0c11300

[29] M.A. Spencer, J. Fortunato, and V. Augustyn, "Electrochemical Proton Insertion Modulates the Hydrogen Evolution Reaction on Tungsten Oxides," Mater. Cloud (2021). https://doi.org/http://doi.org/10.24435/materialscloud:1k-tm